International Journal of Thin Films Science and Technology

http://dx.doi.org/10.18576/ijtfst/150306

Annular Peristaltic Flow for a Non-Newtonian Fluid: Perivascular Space Model Brain

Amina A. Khafagy[1], *Kh. S. Mekheimer*[2,*], *Magdy A. Sirwah*[1], *and A. M. A. Moawad*[2]

[1] Department of Mathematics, Faculty of Science, Tanta University, Tanta, Gharbiea, Egypt
[2] Mathematics Department, Faculty of Science (Boys), Al-Azhar University, Nasr City (11448), Cairo, Egypt

Received: 27 Jun. 2026, Revised: 5 Aug. 2026, Accepted: 8 Aug. 2026
Published online: 1 Sep. 2026

Abstract: The perivascular space (PVS) surrounding cerebral arteries is a major pathway for the transport of cerebrospinal and interstitial fluid and for the clearance of metabolic waste such as amyloid-β. It is also a candidate route for convection-enhanced delivery (CED) of therapeutic agents. We study the peristaltic flow of a Jeffrey fluid in a concentric annular whose gap is filled with a porous (Darcy–Brinkman-type) medium; the inner boundary is the arterial wall carrying a sinusoidal travelling wave. Under the long-wavelength, low-Reynolds-number approximation the problem reduces to a linear boundary-value problem that is solved in closed form in terms of modified Bessel functions. Expressions are obtained for the velocity, the pressure gradient, the pressure rise per wavelength, the time-averaged flow rate and the stream function. The effects of porosity, Darcy permeability, the Jeffrey parameter and the wave amplitude on velocity, pressure rise and the trapped bolus are analyzed, and a dimensionless index PW is introduced to measure how the wall motion modifies the flow driven by the pressure field of a CED needle. The results show that peristaltic wall motion can enhance fluid and solute transport in the PVS, that the Jeffrey parameter and the wave amplitude dominate the response, and that the effects of porosity and permeability are comparatively weaker in the parameter range considered.

Keywords: Jeffrey fluid; Peristaltic wave; Darcy's law; Perivascular space; Hydraulic Permeability; Convection-enhanced delivery.

1 Introduction

The cerebrospinal fluid delivers nutrients and removes metabolic waste, such as amyloid-β. We need to know that the cerebrospinal fluid flowing along the perivascular spaces is an essential part of the brain. Also, it serves as an effective route for administering therapeutic medications to the brain. Some basic concepts of fluid dynamics that are relevant to these flows, as well as the combined effects of solute transport by advection and diffusion (phrase "in the magnet" deleted), were also discussed (Thomas [1]).

Perivascular spaces, also known as Virchow–Robin spaces, are fluid-filled compartments surrounding arteries, veins, and capillaries in the brain. Tracers injected into the brain are transported along the channels surrounding the cerebral blood vessels Wardlaw et al. [2] noted that although these spaces were identified more than 150 years ago, their functional significance has only recently become clearer. Advances in research have indicated that perivascular spaces contribute to the removal of interstitial fluid and metabolic waste from the brain, particularly during sleep, and may be involved in the pathogenesis of small-vessel disease, Alzheimer's disease, other neurological disorders, and inflammatory processes. Experimental models in healthy rodents during sleep and wakefulness have improved understanding of vascular and neurodegenerative brain lesions, sleep patterns, and brain function. Although many aspects remain unknown, current evidence indicates that perivascular spaces play an important role in maintaining brain health (Wardlaw et al. [2]).

In the brain, tracking devices are injected and transported along the channels surrounding the cerebral blood vessels. So, a large flow of fluid was imposed in the channels adjacent to the blood vessels' "glymph" as well as the space surrounding the arteries, and the net flow in these channels was driven by oscillating and constant pressures. It has been found that the movement of the peristaltic wall alone is not sufficient to drive a large flow forward. It has been blending it to explain the shear-enhanced dispersion resulting from the occurrence

* Corresponding author e-mail: kh_Mekheimer@azhar.edu.eg

© 2026 NSP
Natural Sciences Publishing Cor.

of oscillatory pressure in the tangential channels in an analytical manner (M. M. Faghih and M. K. Sharp [3]).

Noreen Sher Akbar and others have come up with a model of Jeffrey's peristaltic flow of chyme in the intestine. In this model, they formulated a problem using two waves. These two sine waves propagate along the outer wall of the tube. However, these two sine waves have wavelengths. Also, these two sine waves are non-periodic. They reached solutions for the increase in velocity and pressure. Also, the physical behaviour of parameters such as velocity, friction force, high blood pressure, and pressure gradient was studied graphically (N. Sher Akbar et al. [4]). Porous media is a candidate to enhance the reduction of pollution formation. Porous media also helps in the penetration efficiency of pollutants such as soot, nitrogen oxides, and carbon dioxide. As a result of preheating of the permeable gases, it is possible to obtain a high temperature in the porous medium (Mohamed [5]).

Microvascular diseases (SVDs) are the result of the occurrence of disorders in the microvascular blood vessels in the brain and also small arteries, veins, and capillaries, (SVDs) cause strokes, and the results worsen after the occurrence of a stroke and there is the main cause of disability, cognitive impairment and impaired mobility, aswell as it has been clarified that the spaces surrounding the blood vessels are the characteristic feature of SVDs, in healthy tissues these spaces form part of the complex myeloid fluid drainage system and may make the removal of negates from the brain Easy operation (Brown et al. [6]).

There is a diversity in diseases of small cerebral blood vessels (SVDs) There is a diversity in diseases of small cerebral blood vessels (SVDs) The etiology of these diseases is widespread but they share diseases significantly, in the hypothesis hypothetical deposits of the brilliant protein are formed and the advantages of the enlarged spaces around (EPVS) as well as the advantages of SVD, it has recently been discovered that the glemfic system provides a treatment to address these gaps where it performs a comprehensive review of the cognitive factors that regulate the function of glemphism and the mechanisms of the disease and that are caused by deficiencies in the glycemphic system with a focus on the importance of The role of the spaces surrounding the blood vessels (PVSs), the cerebral impulse and the physiology of the normal central nervous system (Mestre et al. [7]).

Freitas and others have concluded that the perivascular spaces (PVS) in the brain, sometimes called Virchow-Robin spaces, are made up of cells, fluids, and connective tissue and are limited externally by the stellate feet. An important task of the PVS is to cleanse the brain. The wastes belong to the "periarterial drainage" through the arterial membranes. Brain waste disposal has systems related to the blood-brain barrier, cerebrospinal fluid, meningeal lymphatic vessels, and perineural lymphatic drainage pathways. Therefore, any abnormality that occurs in the PVS leads to the accumulation of waste in the brain. They hypothesized that PVS hypertrophy could be secondary to the accumulation of β-Amyloid, and this leads to a decrease in the strength of the walls of blood vessels and cerebral vasculature (CAA) and hypertrophy of the PVS in the stage that precedes the clinical case of Alzheimer's disease, and also precedes large brain atrophy. They have clarified the advanced concept of PVS systems and brain waste disposal systems, clarifying the importance of dysfunction for cerebrovascular and neurological diseases, as well as clarifying the most important treatment methods (Freitas et al. [8]).

MacLullich et al demonstrated that increased white matter (WM) lesions are associated with cognitive function in the elderly, as enlarged perivascular spaces (EPVS) significantly coexist with WM lesions but it has not been identified, and they have not determined if EPVS is also associated with cognitive function (MacLullich et al. [9]).

Perivascular spaces are well known to help maintain balance and prepare the brain's immune system. However, although researchers have studied these spaces for more than 100 years, many questions remain about the structure around blood vessels in the brain. The purpose of this review is to bring together the research about perivascular spaces in human brain inflammation and in animal models of disease. We explain which types of cells are involved in the shape and function of these spaces and how these areas can be seen. Based on this, we suggest a model of what happens during brain inflammation. We also discuss what is not yet known and the limits of the current research. A better understanding of these spaces could help us learn more about how brain inflammation works and create new ways to treat diseases, like multiple sclerosis (Corey W. Bown et al. [10]).

This paper presents an updated model of Jeffrey's fluid flow within the brain's perivascular space, driven by peristaltic movement. The study explores how the fluid dynamics linked to CED leakage interact with the peristaltic flow of Jeffrey's fluid. The objective is to illustrate the impact of perivascular fluid transport, as captured in CED numerical simulations, on various physiological parameters. Key expressions, including velocity and pressure gradient, have been derived and will be analyzed through graphical representations.

2 Mathematical Description of Model

(PVS) is a thin space filled with fluid that surrounds blood vessels (Figure 1). We use a cylindrical coordinate system where the z-axis is along the center of the vessel. For simplicity, the PVS walls do not allow fluid to pass through. The outer wall stays fixed at $r = R_2$, and the inner wall of the vessel is described by $h(t,z)$. This expression gives the position of a point on the inner wall using the radial coordinate r and the axial coordinate z at time t. The blood vessel moves in a wave-like way,

© 2026 NSP
Natural Sciences Publishing Cor.

represented by $h(t,z) = R_1 + b\sin\big((2\pi/\lambda)(z-ct)\big)$, representing a sinusoidal peristaltic wave. Here, R_1 is the medium radius, b is half-wave amplitude, λ is the wavelength, and c is the wave speed traveling in the positive z-direction. The frequency of a wave is determined using the formula $f = (2\pi)/\lambda$. The perivascular space (PVS), treated as a porous medium, is characterized by a constant porosity, denoted as ε, and a fixed Darcy permeability, represented as κ, which governs its fluid dynamics properties. It is assumed that the Jeffrey fluid saturating the PVS is non-Newtonian, incompressible, and characterized by a constant viscosity μ and density ρ. In the inertial frame of reference, the porous medium moves with a velocity V_{med}, and the governing equation is given by [10,11,12,13].

$$\rho\left(\frac{\partial V}{\partial t}+(V\cdot\nabla)V\right)=\nabla\cdot T - \frac{\varepsilon\mu}{\kappa}(V-V_{med}). \tag{1}$$

The total stress tensor of the Jeffrey fluid is

$$T=-IP+S, \tag{2}$$

$$S=\frac{\mu}{1+\lambda_1}(\dot\gamma+\lambda_2\ddot\gamma), \tag{3}$$

where T and S denote the Cauchy stress tensor and extra stress tensor, respectively, P represents pressure, I is the identity tensor, λ_1 indicates the ratio of relaxation to retardation times, λ_2 is the retardation time, $\dot\gamma$ signifies shear rate, and dots above the quantities denote differentiation with respect to time.

The continuity equation reads:

$$\nabla\cdot V=0. \tag{4}$$

Formatting transformations play a significant role in addressing problems linked to peristalsis, as illustrated in studies like Shapiro et al. [14]. To facilitate analysis, instead of operating within the Σ laboratory frame, where the porous medium (PVS) remains stationary while the peristaltic wave propagates, we transition to the Σ' waveform perspective. In this frame, the peristaltic wave is perceived as stationary, while the porous medium undergoes motion. The coordinate transformation is defined such that $r=R$, $z=Z+ct$, and $\theta=\theta$. The velocity transformations are given as $v_r=u$, $v_\theta=v$, and $v_z=\omega-c$. A key benefit of operating within the wave frame Σ' is that the wave pattern on the inner wall in Σ' can be described as $h(t',z')=R_1+b\sin\big((2\pi/\lambda)z'\big)$, which remains time-independent. Additionally, working in Σ' converts the analysis into a steady-state flow in Σ'. In the Σ' frame, we have:

$$\rho\left[v_r\frac{\partial v_r}{\partial R}+v_z\frac{\partial v_r}{\partial Z}\right]=-\frac{\partial P}{\partial R}+\frac{1}{R}\frac{\partial}{\partial R}(RS_{RR}) + \frac{\partial S_{Rz}}{\partial Z}-\frac{S_{\theta\theta}}{R}-\frac{\varepsilon\mu}{\kappa}v_r. \tag{5}$$

$$\rho\left[v_r\frac{\partial v_z}{\partial R}+v_z\frac{\partial v_z}{\partial Z}\right]=-\frac{\partial P}{\partial Z}+\frac{1}{R}\frac{\partial}{\partial R}(RS_{Rz}) + \frac{\partial S_{zz}}{\partial Z}-\frac{\varepsilon\mu}{\kappa}(v_z+c). \tag{6}$$

Next, we introduce the following non-dimensional quantities:

$$r'=\frac{R}{d},\quad p'=\left(\frac{d^2}{\mu c\lambda}\right)p,\quad S'=\left(\frac{d}{c\mu}\right)S, \quad u=\frac{u'}{c},\quad \omega=\frac{\omega'}{c},\quad z'=\frac{z}{\lambda}. \tag{7}$$

The long-wavelength (lubrication) approximation, usually applied to thin-film flows, is applied here to a porous gap; it is valid for $Re=\left(\frac{\rho cd}{\mu}\right)\ll 1$ and $\beta=\left(\frac{d}{\lambda}\right)\ll 1$. The model equations are:

$$\frac{\partial p'}{\partial r'}=0 \tag{8}$$

$$-\frac{\partial p'}{\partial z'}+\left(\frac{1}{1+\lambda_1}\right)\left[\left(\frac{1}{r'}\right)\frac{\partial\omega'}{\partial r'}+\frac{\partial^2\omega'}{\partial r'^2}\right] -\frac{\varepsilon d^2}{\kappa}(\omega'+1)=0. \tag{9}$$

The boundary condition relevant to the problem:

$$\omega=-1,\quad \text{at } r=\delta,$$
$$\omega=-1,\quad \text{at } r=\eta=\phi+\sigma\sin(2\pi z').$$

Eq. (8) leads to

$$p'=p'(z'). \tag{10}$$

Eq. (9) leads to

$$\omega'(r)=-1-\left(\frac{k}{d^2}\right)\frac{dp'}{dz'}-\left(\frac{k}{A}\right)\frac{dp'}{dz'} \times\Big[Y_0(Br)\big(I_0(C\delta)-I_0(C\eta)\big) +I_0(cr)\big(Y_0(B\eta)-Y_0(B\delta)\big)\Big]. \tag{11}$$

In the Σ' frame, the volumetric flow rate stays unchanged, indicating

$$Q'=\int_{\eta(z')}^{\delta}2\pi r'\omega'\,dr'$$

© 2026 NSP
Natural Sciences Publishing Cor.

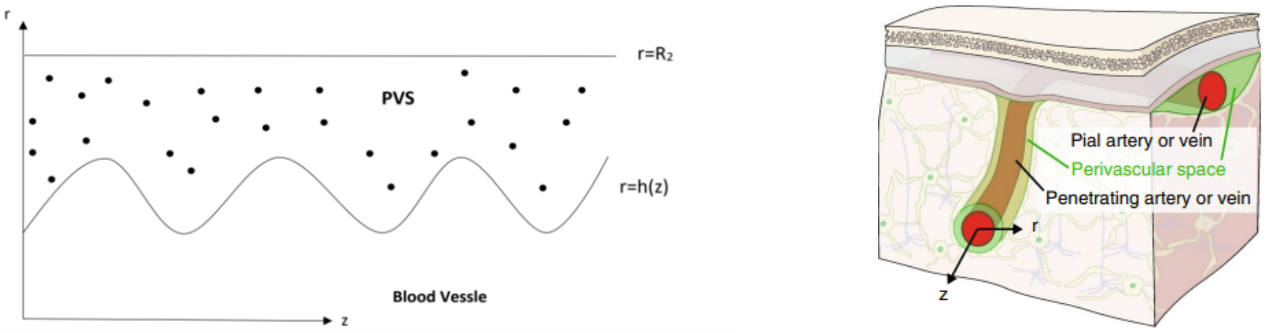


Fig. 1: Geometry of the problem, with a diagram depicting pial and penetrating arteries/veins in the brain and their surroundings perivascular spaces.

does not vary with z'. By substituting Eq. (11) into the flow rate expression, one has:

$$\begin{aligned} Q' = {} & \frac{\pi}{d^3\varepsilon^{3/2}\sqrt{1+\lambda_1}\big(Y_0(B\delta)I_0(C\eta)-I_0(C\delta)Y_0(B\eta)\big)} \\ & \times\Big[\delta\Big(-Dk\delta\frac{dp'}{dz'}{}_0F_1(;2;G\delta^2) \\ & \quad\times\big(Y_0(B\eta)-Y_0(B\delta)\big)\Big) \\ & + I_0(C\delta)\Big(D\delta E\,Y_0(B\eta) \\ & \quad - 2ik^{3/2}\frac{dp'}{dz'}Y_1(B\delta)\Big) \\ & + I_0(C\eta)\Big(2ik^{3/2}\frac{dp'}{dz'}Y_1(B\delta) \\ & \quad - \delta DE\,Y_0(B\delta)\Big)\Big] \\ & + D\eta^2\Big[-k\frac{dp'}{dz'}{}_0F_1(;2;G\eta^2) \\ & \quad\times\big(Y_0(B\delta)-Y_0(B\eta)\big) \\ & \quad + E\,Y_0(B\delta)I_0(C\eta) \\ & \quad - E\,I_0(C\delta)Y_0(B\eta)\Big] \\ & + ik^{3/2}\frac{dp'}{dz'}\,\eta\,Y_1(B\eta) \\ & \quad\times\big(I_0(C\delta)-I_0(C\eta)\big)\Big]. \end{aligned} \tag{12}$$

Consequently, Eq. (12) gives:

$$\frac{dp'}{dz'} = \frac{\pi\delta^2+Q-\pi\eta^2}{M} \tag{13}$$

Since $\eta(z')$ is an aperiodic function of z' that repeats at intervals of λ, Eq. (13) indicates that $\dfrac{dp'}{dz'}$ is also a periodic function of z' with the same period, λ. Therefore, integrating $\dfrac{dp'}{dz'}$ over an interval of length λ with respect to z' yields a constant value, $\Delta p'_\lambda$ which is independent of the interval's starting point. A simple series of computations produces the following expression for $\Delta p'_\lambda$:

$$\begin{aligned} \Delta p'_\lambda = 2\Bigg(& \frac{\pi\delta^2-\pi C_1^2+Q}{C_5}+\frac{\pi\delta^2C_2^2+Q}{C_6} \\ & + \frac{\pi\delta^2-\pi C_3^2+Q}{C_7}+\frac{\pi\delta^2-\pi C_4^2+Q}{C_8}\Bigg) \\ & + \frac{2(\pi\delta^2-\pi\phi^2+Q)}{C_9}. \end{aligned} \tag{14}$$

In the Σ frame, we note that the pressure changes for each wavelength $\Delta p_\lambda = \Delta p'_\lambda$. The volumetric flow rate, evaluated at time t and at an axial position z, can be expressed as follows:

$$\begin{aligned} Q(t,z) &= 2\pi\int_{\eta(t,z)}^{\delta}\varepsilon\omega' r\,dr = 2\pi\varepsilon\int_{\eta(t,z)}^{\delta}(\omega+c)r\,dr \\ &= \frac{1}{2}\varepsilon Q' + \pi\varepsilon c(\delta^2-\eta^2), \end{aligned}$$

where $\eta = \phi+\sigma\sin\big(2\pi(z-ct)\big)$. By incorporating these results into Eq. (14) and proceeding to solve for $Q(t,z)$.

The time-averaged flow rate can be expressed as

$$\overline{Q}(z) = \left(\frac{1}{T}\right)\int_0^T Q(t,z)\,dt.$$

Through the application of straightforward calculations, it can be determined that the volumetric flow rate remains invariant with respect to the variable z and is expressed as

$$\overline{Q} = \frac{1}{T}\big[\,\xi+\zeta\,\big]. \tag{15}$$

The explicit expressions of ξ and ζ are omitted for brevity and are available from the corresponding author upon reasonable request.

© 2026 NSP
Natural Sciences Publishing Cor.

We can also find the stream function with it $\psi = -\int_{h(z')}^{\delta} \omega'(z')\,dr$.

$$\begin{aligned}\psi(r,z) = \frac{1}{2A}\Bigg[r\Bigg(& \kappa P_z r\,{}_0F_1\left(;2;\varepsilon r^2 G\right) \\ & \times \left(Y_0(\delta B) - Y_0(\eta B)\right) \\ & - r\left(\varepsilon d^2 + \kappa P_z\right) \\ & \times \left(Y_0(\delta B) I_0(C\eta) - I_0(C\delta) Y_0(B\eta)\right) \\ & + \frac{2iP_z\kappa^{3/2} Y_1(Br)\left(I_0(C\eta) - I_0(B\eta)\right)}{D}\Bigg) \\ - \eta\Bigg(& \kappa P_z r\,{}_0F_1\left(;2;H\eta^2\right) \\ & \times \left(Y_0(\delta B) - Y_0(\eta B)\right) \\ & - \eta\left(\varepsilon d^2 + \kappa P_z\right) \\ & \times \left(Y_0(\delta B) I_0(C\eta) - I_0(C\delta) Y_0(B\eta)\right) \\ & + \frac{2iP_z\kappa^{3/2} Y_0(B\eta)\left(I_0(C\eta) - I_0(C\delta)\right)}{D}\Bigg)\Bigg] + Q. \end{aligned} \tag{16}$$

where

$$h(z') = \phi + \sigma\sin(2\pi z').$$

3 Results and Discussion

The initial application of the lubrication approximation simplified the system by reducing the number of non-linear equations and converting them into linear equations, which are solvable via the superposition principle. Consequently, it is consistently inferred that the volumetric flow rate is influenced by the combined effects of the boundary's peristaltic motion and the pressure gradient. In the moving frame, the governing equation is homogeneous (Eq. (9)), whereas in the laboratory frame, the boundaries exhibit dynamic behavior. In this scenario, the superposition principle is inapplicable in both frameworks. Notably, the pressure gradient establishes a coupling between the flow field and the peristaltic wave. This section presents the graphical results and provides a physical interpretation of the various parameters involved in the solutions. Symbols utilized in the analysis not previously mentioned are enumerated in Table 1.

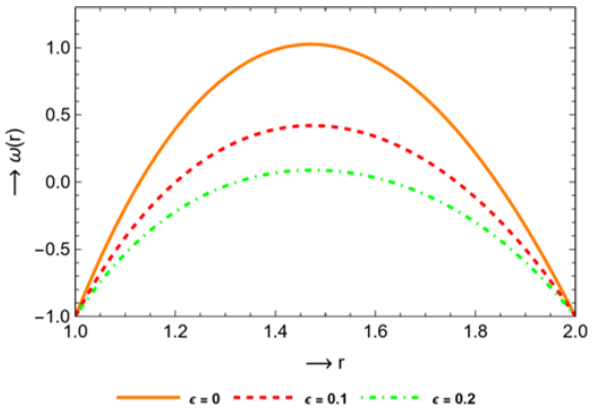


Fig. 2: Velocity for different values of porosity of the medium ε, the other parameters are $\phi = 1, \delta = 2, \sigma = 0.01, z' = 0.5, \lambda_1 = 1, k = 0.002, p_z = 8$.

In the beginning, we find that ω it is a function of r, and we will study the effect of some factors on the speed.

Figure 2 depicts the influence of the medium porosity parameter ε on the axial velocity distribution $\omega(r)$. The graphical representation clearly demonstrates an inverse correlation between the porosity parameter ε and the fluid speed. As the porosity parameter increases from 0 to 0.2, the velocity curves exhibit a continuous downward shift across the channel width. From a physical standpoint, an increase in porosity enhances the internal drag forces and flow resistance within the porous matrix, which dissipates the fluid's kinetic energy and consequently decelerates the flow. In addition, the speed reaches its highest value in the middle of the channel and decreases smoothly towards both walls.

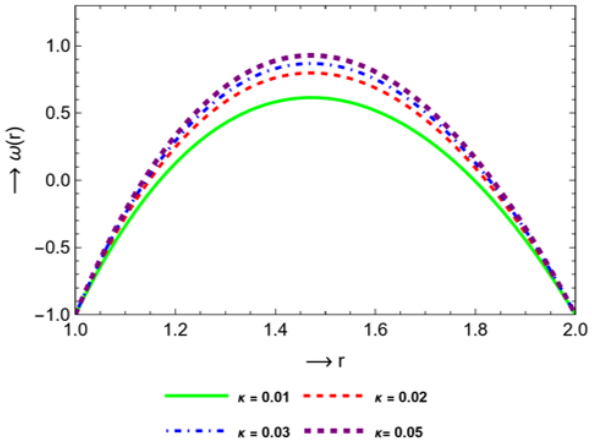


Fig. 3: Velocity for different values of Darcy permeability k, the other parameters are $\phi = 1, \delta = 2, \sigma = 0.01, z' = 0.5, \lambda_1 = 1, \varepsilon = 0.3, p_z = 8, d = 0.2$.

© 2026 NSP
Natural Sciences Publishing Cor.

Table 1: Naming conventions for the parameters and variables.

Symbol	Physical Meaning
R_1	inner radius
R_2	Outer radius
b, σ	Half amplitude
λ_1, J	Wavelength
c	Wave speed
k	Darcy permeability
K	Hydraulic permeability ($=\frac{k}{\mu}$)
f	Wave frequency
T	Period of the wave
ρ	fluid Density
v	Fluid velocity (distinct from the superficial velocity)
P	Fluid Pressure
ε	Medium porosity

Figure 3 illustrates the impact of Darcy permeability k on the axial velocity distribution $\omega(r)$. It is evident that an increase in k (from 0.01 to 0.05) leads to a noticeable rise in the fluid speed across the channel. Physically, higher permeability reduces the medium's resistance to fluid flow, allowing the fluid to move more freely and enhancing its overall speed.

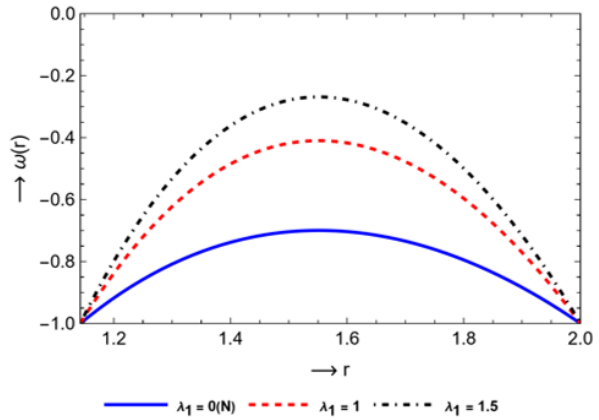


Fig. 4: Velocity corresponding to various values of λ_1, the rest of the parameters are held fixed at the values $\phi = 1, \delta = 2, \sigma = 0.15, z' = 0.2, k = 0.051, \varepsilon = 0.3, p_z = 3.3, d = 0.2$.

In Figure 4, the influence of the Jeffrey fluid parameter λ_1 on the axial velocity $\omega(r)$ is presented. It is clear that the fluid speed increases proportionally with higher values of λ_1. Transitioning from the Newtonian case ($\lambda_1 = 0$) to non-Newtonian behavior ($\lambda_1 = 1,\ 1.5$) causes a substantial elevation in the velocity profile across the entire channel width. Physically, an increase in λ_1 reduces the internal flow resistance under a constant pressure gradient, thereby accelerating the fluid movement and enhancing its maximum velocity at the channel center ($r \approx 1.5$).

Figure 5 shows how the pressure increase Δp changes with the flow rate Q for values of Darcy permeability k. The results show that as k goes up from 0.01 to 0.1, the pressure gradient curves move downward. This happens because higher permeability means resistance to flow in the porous material. So less pressure difference is needed to keep the moving.

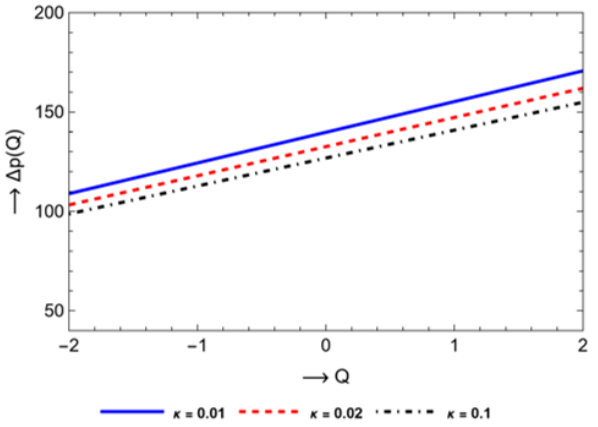
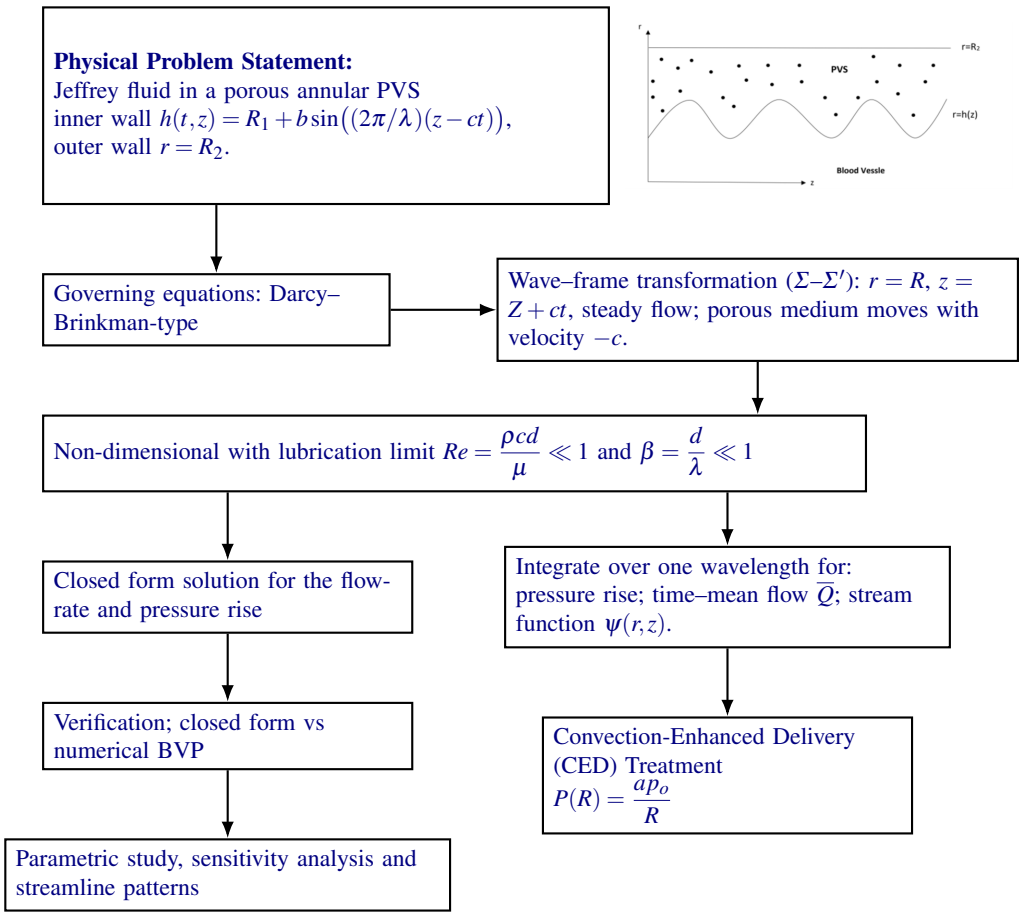


Fig. 5: Pressure gradient Δp with selected values of Darcy permeability k, the other parameters are $\phi = 1, \delta = 2, \sigma = 0.2, z' = 0.5, \lambda_1 = 0.01, d = 0.2, \varepsilon = 0.3$.

Figure 6 illustrates the variation of pressure rise per wavelength, Δp, versus flow rate Q for different values of the Jeffrey fluid parameter λ_1. As λ_1 increases from 0 (Newtonian baseline) to 0.4, the pressure difference Δp decreases noticeably across all flow rates, confirming an inverse relationship. Physically, higher values of λ_1 reduce internal shear resistance within the viscoelastic fluid, which subsequently lowers the required pressure difference to propel the fluid flow. Figure 7 depicts the effect of the medium porosity parameter ε on the pressure rise Δp. The results reveal a proportional correlation; increasing ε leads to a notable elevation in the Δp profiles across all values of Q. This increase occurs because a

© 2026 NSP
Natural Sciences Publishing Cor.

Model Flow Charts:



more porous medium exerts higher hydraulic resistance on the flow, requiring a greater pressure force to drive the fluid.

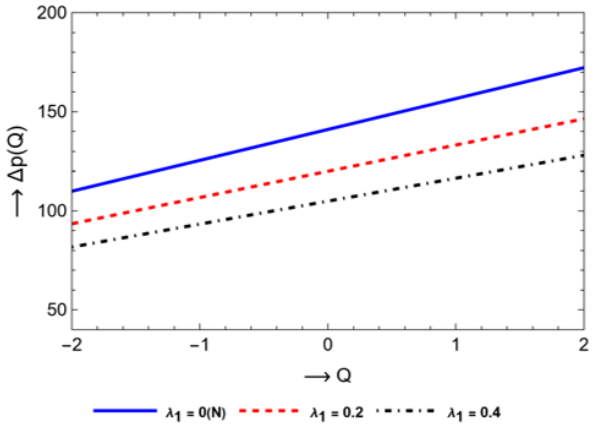


Fig. 6: Pressure gradient Δp for different values of the parameter λ_1, the other parameters are $\phi = 1, \delta = 2, \sigma = 0.2, z' = 0.5, k = 0.01, \varepsilon = 0.3, d = 0.2$.

Figure 8 presents the streamline patterns, represented by the stream function ψ, in the $r-z$ plane for different values of the parameter λ_1 of the Jeffrey fluid, specifically 0, 1, and 1.5. It is evident that as λ_1 increases, the size of the trapped bolus significantly enlarges and becomes more distinct.

In Figure 9, the streamline patterns for different values of Darcy permeability $k = 0.051$, 0.55, and 0.8 are presented. A clear expansion in the trapped bolus size is observed as k increases. Specifically, the region bounded by $\Psi = 0.5$ widens, and deeper closed streamlines ($\Psi = 0.8$) emerge at higher permeability values. Physically, increasing k reduces flow resistance, thereby promoting fluid circulation and enhancing the trapping phenomenon. Figure 10 illustrates the streamline patterns of the stream function ψ in the $r-z$ plane for different porosity values ($\varepsilon = 0.03$ and 0.4). A noticeable shrinkage in the trapped bolus size is observed as the porosity parameter ε increases. Specifically, the region enclosed by $\psi = 0.55$ contracts, and the inner deep contour loops ($\psi = 0.8$) disappear. Physically, higher medium porosity introduces additional drag resistance,

© 2026 NSP
Natural Sciences Publishing Cor.

which suppresses fluid circulation and reduces the volume of the trapped bolus.

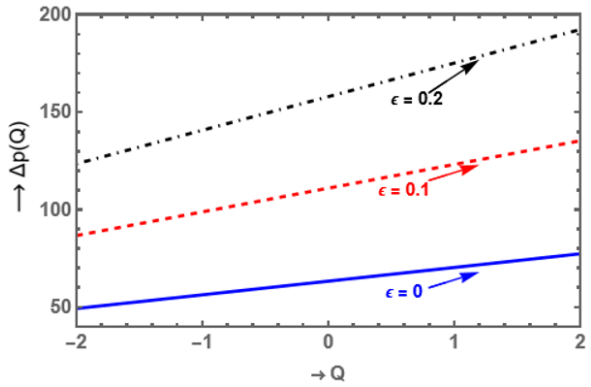


Fig. 7: Pressure gradient Δp for different values of porosity ε, the other parameters are $\phi = 1, \delta = 2, d = 0.2, \sigma = 0.2, z' = 0.5, k = 0.001, \lambda_1 = 1$.

Figure 11 illustrates the streamline patterns of the stream function ψ in the $r - z$ plane for values of the wave half-amplitude ($\sigma = 0.1$ and 0.3). A clear expansion in the trapped size is observed with increasing wave half-amplitude σ. Physically, a larger wave amplitude enhances the pumping force and wall deformation, which promotes fluid entrapment and enlarges the circulating bolus volume.

4 Convection-Enhanced Delivery (CED) Treatment

In the introduction we outlined our focus on investigating the interplay between the behavior of the vascular wall and the efficiency of convection-enhanced delivery (CED). The treatment process for CED involves the administration of medication into the brain tissue either through an implanted catheter or via a needle. Because the brain tissue is elastic, it retracts when it leaks out under high pressure at the needle tip. This retraction creates a fluid-filled cavity at the needle exit, from which the injected fluid moves into the nearby tissue. As a result, a tiny pressure field forms around the point source, at the needle outlet. (Neeves et al. [15]).

$$P(R) = \frac{ap_o}{R} \tag{17}$$

The pressure p_o inside the needle tip is expressed as a function of the radial distance R from the sources. A typical value for p_o is 7 kPa, while a is 13 μm. At location R, the microscopic pressure gradient is oriented radially relative to the source position, is

$$\frac{dP}{dR} = \frac{-ap_o}{R^2} \tag{18}$$

The effect of the vessel's wave-like motion and the pressure from CED depends on how the blood vessel is positioned. If the vessel is at a right angle to the radial direction, the pressure from CED is almost zero. But if the vessel is arranged along the radius and the wave moves outward, the pressure inside the PVS changes in a special way. Under these conditions, the pressure change per wavelength, denoted as Δp_λ, can be calculated using the equation $\left(\frac{-ap_o}{R^2}\right) J$. This outcome highlights that Q is dependent on R for the examined blood vessels, providing a basis to evaluate the impact of CED treatment both in the presence and absence of peristaltic activity within the vessel walls. We determine the following number, and it is dimensionless:

$$PW(R) = \frac{\overline{Q}(R) - \overline{Q}(R)|_{b=0}}{\overline{Q}(R)} \times 100. \tag{19}$$

The term "PW" refers to "Peristaltic Wave," while "R" is defined as e raised to the power of θ. The Peristaltic Wave, or PW, is dependent on θ, and we will explore the impact of different parameter values.

The analysis presented in Fig. 12 shows that an increase in the Darcy permeability parameter (κ) results in a decrease in the peristaltic wave function $PW(\theta)$. In contrast, Fig. 13 demonstrates that an increase in the half amplitude parameter (σ) leads to an increase in the peristaltic wave function $PW(\theta)$.

5 Conclusion

–A mathematical model for Jeffrey fluid flow in the cerebral PVS was developed.

–Increasing the Jeffrey parameter (λ_1) enhances velocity and fluid trapping, while decreasing the pressure gradient.

–Increasing the porosity (ε) reduces velocity and fluid trapping, while increasing the pressure gradient.

–Increasing Darcy Permeability (κ) enhances velocity and fluid trapping, while decreasing the pressure gradient.

–Increasing the wave amplitude (b) enhances the size of the trapped bolus and peristaltic pumping.

–Peristaltic motion of blood vessel walls actively drives fluid and drug transport within the perivascular space (PVS).

–The model provides a theoretical framework for understanding PVS transport and its interaction with CED.

© 2026 NSP
Natural Sciences Publishing Cor.

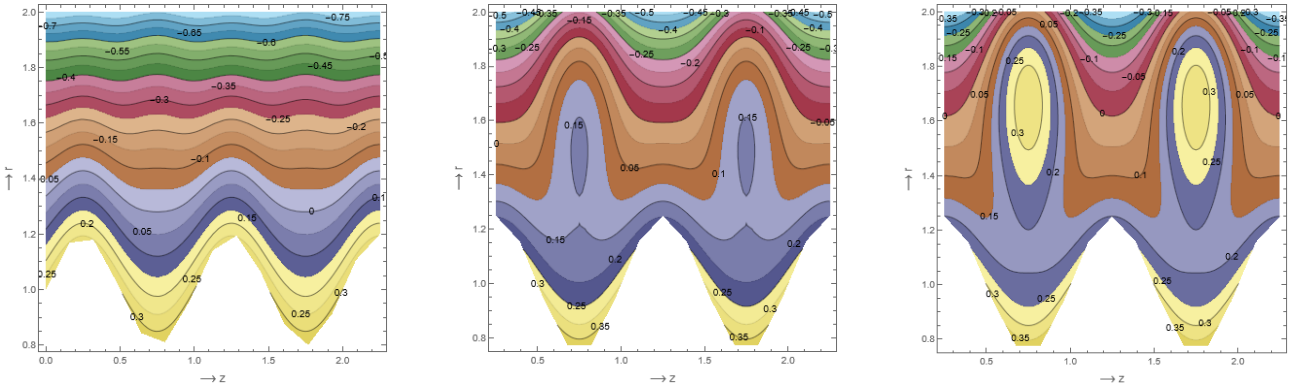


Fig. 8: Stream function at λ_1, $\lambda_1 = 0,\ 1$ and 1.5 the other parameters are $\phi = 1, \delta = 2, \sigma = 0.15, k = 0.051, Q = 0.3, \varepsilon = 0.3, d = 0.2,\ P_z = -3.3$

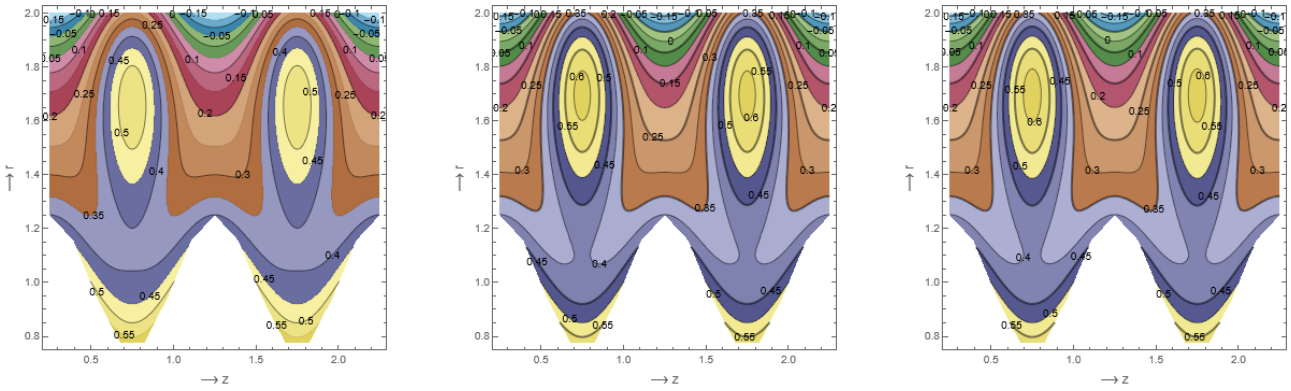


Fig. 9: Stream function for different values of Darcy permeability k, $k = 0.051,\ 0.55$ and 0.8 the other parameters are $\phi = 1, \delta = 2, \sigma = 0.15, \lambda_1 = 1.5, Q = 0.3, \varepsilon = 0.3, d = 0.2,\ P_z = -3.3$



Fig. 10: Stream function for different values of the Porosity of the medium ε, $\varepsilon = 0.03$ and 0.4, the other parameters are $\phi = 1, \delta = 2, \sigma = 0.15, \lambda_1 = 1.5, Q = 0.3, d = 0.2, k = 0.051,\ P_z = -3.3$

© 2026 NSP
Natural Sciences Publishing Cor.



Fig. 11: Stream function for different values of Half amplitude $\sigma, \sigma = 0.1$ and 0.3, the other parameters are $\phi = 1, \delta = 2, d = 0.2, \lambda_1 = 1.5, Q = 0.3, \varepsilon = 0.3, k = 0.051,\ P_z = -3.3$

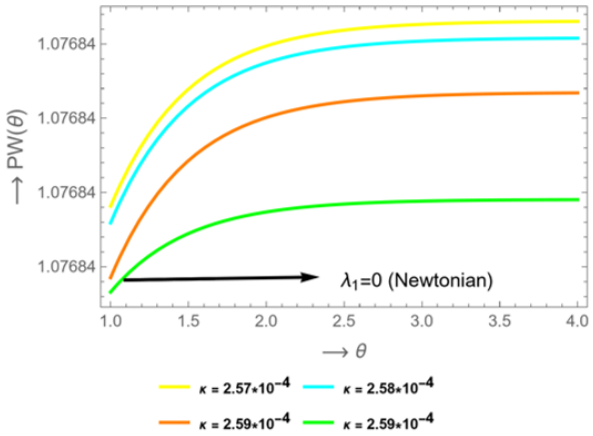


Fig. 12: The Peristaltic Wave (PW) for different values of parameter Darcy permeability parameter k, the other parameters are $\phi = 1, \delta = 1.02, \varepsilon = 2.2 \times 10^{-5}, \sigma = 0.8, d = 0.02, T = 2\pi, a = 0.13, p_o = 0.15, c = 2.5, J = 1, \lambda_1 = 1, z' = 0.5$

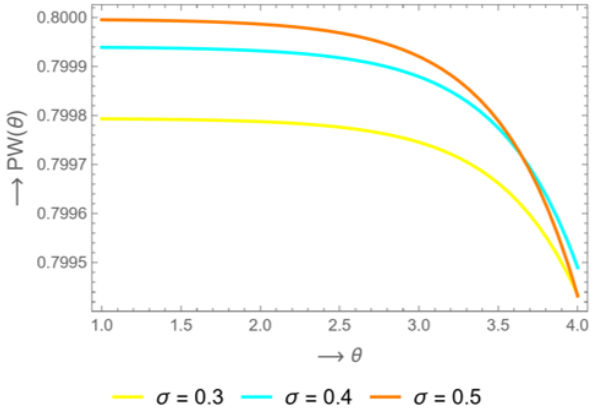


Fig. 13: The Peristaltic Wave PW for different values of the parameter Half amplitude σ, the other parameters are $\phi = 1, \delta = 1.02, \varepsilon = 0.0077, k = 5 \times 10^{-9}, T = 2\pi, d = 0.02, a = 0.13, p_o = 0.15, c = 2.5, J = 1, \lambda_1 = 1, z' = 0.5$

© 2026 NSP
Natural Sciences Publishing Cor.

References

[1]Thomas John H.; Fluid dynamics of cerebrospinal fluid flow in perivascular spaces. *Journal of the Royal Society Interface.* 2019, 16(159), 20190572.

[2]Wardlaw Joanna M.; Benveniste H.; Nedergaard M.; Zlokovic Berislav V.; Mestre H.; Lee H,; Doubal Fergus N.;, Brown R.; Ramirez J.; MacIntosh J. Perivascular spaces in the brain: anatomy, physiology and pathology. *Nature Reviews Neurology.* 2020, 16(3), 137–153.

[3]Faghih M.; Sharp M K. Mechanisms of tracer transport in cerebral perivascular spaces. *Journal of biomechanics.* 2021, 118, 110278.

[4]Sher Akbar N.; Nadeem S.; Lee C. Characteristics of jeffrey fluid model for peristaltic flow of chyme in small intestine with magnetic field. *Results in Physics.* 2013, 3, 152–160.

[5]Mohamad A.A. combustion in porous. *Transport phenomena in porous media III.* 2005, 3:287,.

[6]Brown R.; Benveniste H.; Black E.; Charpak S.; Dichgans M. Anne Joutel, Nedergaard M.; Smith J.; Zlokovic V.; Wardlaw Joanna M. Understanding the role of the perivascular space in cerebral small vessel disease. *Cardiovascular research.* 2018, 114(11), 1462–1473,.

[7]Mestre H.; Kostrikov S.; Mehta Rupal I.; Nedergaard Maiken. Perivascular spaces, glymphatic dysfunction, and small vessel disease. *Clinical science*, 131(17), 2257–2274, 2017.

[8]Gouveia-Freitas K.; Bastos António J -L. Perivascular spaces and brain waste clearance systems: relevance for neurodegenerative and cerebrovascular pathology. *Neuroradiology*, 2021, 63(10), 1581–1597.

[9]MacLullich J.; Wardlaw M.; Ferguson J.; Starr M.; Seck R.; and Deary J. Enlarged perivascular spaces are associated with cognitive function in healthy elderly men. *Journal of Neurology, Neurosurgery & Psychiatry.* 2004, 75(11), 1519–1523,

[10]Brinkman H C. A calculation of the viscous force exerted by a flowing fluid on a dense swarm of particles. *Flow, Turbulence and Combustion*. 1949, 1(1), 27–34,.

[11]William Murray. Analysis of transport Phenomena.(No Title), 1998.

[12]Inna Ya Edelman. Wave dynamics of saturated porous media and evolutionary equations. *Transport in porous media*, 34(1):117–128, 1999.

[13]Peng Wang and William L Olbricht. Fluid mechanics in the perivascular space. Jornal of theoretical biology, 274(1):52–57, 2011.

[14]Ascher H Shapiro, Michel Yves Jaffrin, and Steven Louis Weinberg. Peristaltic pumping with long wavelengths at low reynolds number. *Journal of fluid mechanics*, 37(4):799–825, 1969.

[15]KB Neeves, CT Lo, CP Foley, WM Saltzman, and WL Olbricht. Fabrication and characterization of microfluidic probes for convection enhanced drug delivery. *Journal of controlled release*, 111(3):252–262, 2006.

[16]Donald A Nield and Adrian Bejan. *Convection in porous media*. Springer, 2006.

© 2026 NSP
Natural Sciences Publishing Cor.

Appendix A

$$\eta(z') = \phi + \sigma \sin(2\pi z')$$
$$d = R_2 - R_1, \quad \phi = \frac{R_1}{d}, \quad \delta = \frac{R_2}{d}, \quad \sigma = \frac{b}{d}, \quad A = d^2\varepsilon\left[I_0(C\eta)Y_0(B\delta) - I_0(C\delta)Y_0(B\eta)\right]$$
$$B = \frac{-id\sqrt{1+\lambda_1}\sqrt{\varepsilon}}{\sqrt{k}}, \quad C = \frac{d\sqrt{\varepsilon(1+\lambda_1)}}{\sqrt{k}}, \quad D = d\sqrt{\varepsilon}\sqrt{1+\lambda_1}, \quad E = d^2\varepsilon + k\frac{dp'}{dz'},$$
$$G = \frac{d^2(1+\lambda_1)}{4k}, \quad H = \frac{d^2\varepsilon(1+\lambda_1)}{4k}$$

$$M = \frac{2i\pi k^{3/2}\left[\delta Y_1(B\delta) - \eta Y_1(B\eta)\right]\left[I_0(C\delta)I_0(C\eta)\right]}{d^3\varepsilon^{3/2}\sqrt{1+\lambda_1}\left[Y_0(B\delta)I_0(C\eta) - I_0(C\delta)Y_0(B\eta)\right]} + \frac{\pi\delta^2 k}{d^2\varepsilon}$$
$$+ \frac{\pi k\left[\delta^2\,{}_0F_1(;2;H\delta^2) - \eta^2\,{}_0F_1(;2;H\eta^2)\right]\left[Y_0(B\eta) - Y_0(B\delta)\right]}{d^2\varepsilon\left[Y_0(B\delta)I_0(C\eta) - I_0(C\delta)Y_0(B\eta)\right]} - \frac{\pi k\eta^2}{d^2\varepsilon}$$

$$N = \frac{0.25\,(\lambda_1+1)\,c_{11}^2\,\varepsilon}{k}$$

$$\begin{aligned} W = \pi k\Big[&-iY_0(ER_2)\,{}_0F_1(;2;HR_2^2)R_2^3 + Y_0(ER_2)\,{}_0F_1(;1;H\eta^2)iR_2^3 \\ &- iR_1Y_0(ER_2)\,{}_0F_1(;1;H\eta^2)R_2^2 + R_1Y_0(ER_2)\,{}_0F_1(;2;HR_2^2)iR_2^2 \\ &- 2iR_2\sqrt{k}Y_1(ER_2)\left({}_0F_1(;1;HR_2^2) - {}_0F_1(;1;H\eta^2)\right) \\ &- i\eta^2Y_0(ER_2)\,{}_0F_1(;1;H\eta^2)R_2 + \eta^2Y_0(ER_2)\,{}_0F_1(;2;H\eta^2)iR_2 \\ &- 2i\eta\sqrt{k}Y_1(E\eta)\,{}_0F_1(;1;H\eta^2) - iR_1\eta^2Y_0(ER_2)\,{}_0F_1(;2;H\eta^2) \\ &+ R_1\eta^2Y_0(ER_2)\,{}_0F_1(;1;H\eta^2)i + \Delta R\,iY_0(E\eta)\left(\eta^2\,{}_0F_1(;2;H\eta^2)\right. \\ &\left.+ (R_2^2 - \eta^2)\,{}_0F_1(;1;HR_2^2)\right) - {}_0F_1(;2;HR_2^2)R_2^2 + 2i\sqrt{k}\,\eta\,Y_1\left(E\eta\,{}_0F_1(;1;HR_2^2)\right)\Big] \end{aligned}$$

$$c_1 = \phi - 0.9510565162951536\,\sigma, \qquad c_2 = \phi - 0.587785252292473\,\sigma,$$
$$c_3 = \phi + 0.5877852522924732\,\sigma\phi, \qquad c_4 = \phi + 0.9510565162951536\,\sigma$$

© 2026 NSP
Natural Sciences Publishing Cor.

$$c_5 = \frac{\pi\delta^2 k}{d^2\varepsilon} - \frac{\pi c_1^2 k}{d^2\varepsilon} + \frac{2i\pi k^{3/2}\big(I_0(C\delta) - I_0(Cc_1)\big)\big(\delta Y_1(B\delta) - c_1 Y_1(Bc_1)\big)}{d^3\varepsilon^{3/2}\sqrt{1+\lambda_1}\big(I_0(Cc_1)Y_0(B\delta) - I_0(C\delta)Y_0(Bc_1)\big)} + \frac{\pi k\big(Y_0(Bc_1) - Y_0(B\delta)\big)\big({}_0F_1(;2;H\delta^2)\delta^2 - {}_0F_1(;2;Hc_1^2)c_1^2\big)}{d^2\varepsilon\big(I_0(Cc_1)Y_0(B\delta) - I_0(C\delta)Y_0(Bc_1)\big)}$$

$$c_6 = \frac{\pi\delta^2 k}{d^2\varepsilon} - \frac{\pi c_2^2 k}{d^2\varepsilon} + \frac{2i\pi k^{3/2}\big(I_0(C\delta) - I_0(Cc_2)\big)\big(\delta Y_1(B\delta) - c_2 Y_1(Bc_2)\big)}{d^3\varepsilon^{3/2}\sqrt{1+\lambda_1}\big(I_0(Cc_2)Y_0(B\delta) - I_0(C\delta)Y_0(Bc_2)\big)} + \frac{\pi k\big(Y_0(Bc_2) - Y_0(B\delta)\big)\big({}_0F_1(;2;H\delta^2)\delta^2 - {}_0F_1(;2;Hc_2^2)c_2^2\big)}{d^2\varepsilon\big(I_0(Cc_2)Y_0(B\delta) - I_0(C\delta)Y_0(Bc_2)\big)}$$

$$c_7 = \frac{\pi\delta^2 k}{d^2\varepsilon} - \frac{\pi c_3^2 k}{d^2\varepsilon} + \frac{2i\pi k^{3/2}\big(I_0(C\delta) - I_0(Cc_3)\big)\big(\delta Y_1(B\delta) - c_3 Y_1(Bc_3)\big)}{d^3\varepsilon^{3/2}\sqrt{1+\lambda_1}\big(I_0(Cc_3)Y_0(B\delta) - I_0(C\delta)Y_0(Bc_3)\big)} + \frac{\pi k\big(Y_0(Bc_3) - Y_0(B\delta)\big)\big({}_0F_1(;2;H\delta^2)\delta^2 - {}_0F_1(;2;Hc_3^2)c_3^2\big)}{d^2\varepsilon\big(I_0(Cc_3)Y_0(B\delta) - I_0(C\delta)Y_0(Bc_3)\big)}$$

$$c_8 = \frac{\pi\delta^2 k}{d^2\varepsilon} - \frac{\pi c_4^2 k}{d^2\varepsilon} + \frac{2i\pi k^{3/2}\big(I_0(C\delta) - I_0(Cc_4)\big)\big(\delta Y_1(B\delta) - c_4 Y_1(Bc_4)\big)}{d^3\varepsilon^{3/2}\sqrt{1+\lambda_1}\big(I_0(Cc_4)Y_0(B\delta) - I_0(C\delta)Y_0(Bc_4)\big)} + \frac{\pi k\big(Y_0(Bc_4) - Y_0(B\delta)\big)\big({}_0F_1(;2;H\delta^2)\delta^2 - {}_0F_1(;2;Hc_4^2)c_4^2\big)}{d^2\varepsilon\big(I_0(Cc_4)Y_0(B\delta) - I_0(C\delta)Y_0(Bc_4)\big)}$$

$$c_9 = \frac{\pi\delta^2 k}{d^2\varepsilon} - \frac{\pi\phi^2 k}{d^2\varepsilon} + \frac{2i\pi k^{3/2}\big(I_0(C\delta) - I_0(C\phi)\big)\big(\delta Y_1(B\delta) - \phi Y_1(B\phi)\big)}{d^3\varepsilon^{3/2}\sqrt{1+\lambda_1}\big(I_0(C\phi)Y_0(B\delta) - I_0(C\delta)Y_0(B\phi)\big)} + \frac{\pi k\big(Y_0(B\phi) - Y_0(B\delta)\big)\big({}_0F_1(;2;H\delta^2)\delta^2 - {}_0F_1(;2;H\phi^2)\phi^2\big)}{d^2\varepsilon\big(I_0(C\phi)Y_0(B\delta) - I_0(C\delta)Y_0(B\phi)\big)}$$

$$c_{10} = 6.283185307179586, \qquad c_{11} = 3.141592653589793, \qquad c_{12} = 0 + 1\cdot i$$

$$c_{13} = \frac{\pi\delta^2 k}{d^2\varepsilon} - \frac{c_{11}c_2^2 k}{d^2\varepsilon} + \frac{c_{10}ik^{3/2}\big[I_0(c_{12}c\delta) - 1'I_0(Cc_2)\big]\big[\delta Y_1(C\delta) - c_2 Y_1(-c_{12}c_2 C)\big]}{d^3\varepsilon^{3/2}\sqrt{1+\lambda_1}\big[I_0(Cc_2)Y_0(c_{12}C\delta) - 1'I_0(C\delta)Y_0(-c_{12}c_2 C)\big]} + \frac{\pi k\big[Y_0(-c_{12}c_2 C) - 1'Y_0(-c_{12}C\delta)\big]\Big[\delta^2\,{}_0F_1\big(;2;\frac{0.25d^2\delta^2\varepsilon(\lambda_1+1')}{k}\big) - 1'c_2^2\,{}_0F_1\big(;2;\frac{0.25d^2\varepsilon c_2^2(\lambda_1+1')}{k}\big)\Big]}{d^2\big[\varepsilon I_0(Cc_2)Y_0(c_{12}C\delta) - 1'\varepsilon I_0(\delta C)Y_0(-c_{12}c_2 C)\big]}$$

$$\begin{aligned} c_{14} = 4\pi\Big(&d\big(I_0(C\delta)Y_0(B\eta) - I_0(C\eta)Y_0(B\delta) + (Y_0(B\delta)Y_0(B\eta)\,{}_0F_1(;2;H\eta^2)\big)\sqrt{\varepsilon}\sqrt{1+\lambda_1}\,\eta^2 \\ &- 2i\sqrt{k}\big(I_0(C\delta) - I_0(c\eta)\big)Y_0(B\eta)\,\eta + \delta\big(I_0(C\delta)(2i\sqrt{k}Y_1(B\delta) - D\delta Y_0(B\eta)) \\ &+ I_0(C\eta)(\delta D Y_0(B\delta) - 2i\sqrt{k}Y_1(B\delta)) + d\delta\big(Y_0(B\eta)\,{}_0F_1(;2;H\delta^2)\sqrt{\varepsilon}\sqrt{1+\lambda_1}\big)\big)\Big) \end{aligned}$$

© 2026 NSP
Natural Sciences Publishing Cor.